ROYAL SOCIETY
OF CHEMISTRY

EDGE ARTICLE

Check for updates

Bulky alkali metal cations enabled highly efficient iridium-catalyzed asymmetric hydrogenation for C–N axial chirality *via* dynamic kinetic resolution

Xianghua Zhao,[a] Xinyu Chen,[a] Linxian Fan,[a] Yulong Jiang,[a] Yirui Chen,[a] Dingguo Song,[c] Fei Ling, [ID] *[a] Junyuan Hu [ID] *[b] and Weihui Zhong [ID] *[a]

The addition of excess alkali metal to Noyori-type catalysts (HM–NH) generates anionic species (HM–NM′), which significantly enhances both the reaction rate and turnover number (TON) in asymmetric hydrogenation. However, such anionic catalysts have been largely confined to the construction of central chirality, with few reports on application to axial chirality. Herein, we report a highly efficient anionic iridium catalyst (**HIr-NCs**) based on a newly tridentate ligand framework (**Huaphos**), which enables the asymmetric hydrogenation of *N*-aryl indole ketones (and aldehydes) *via* dynamic kinetic resolution under mild conditions, allowing for the construction of axial chirality with excellent stereocontrol (up to >99% ee and >99 : 1 dr). DFT studies indicate that strong electrostatic interaction between the bulky cesium cation and the oxygen atom of the substrate dramatically reduces the activation barrier, resulting in a substantially accelerated reaction rate for the anionic Ir catalyst (**HIr-NCs**) compared to the neutral **Ir/Huaphos** system (**HIr-NH**). In the presence of anionic Ir catalyst, this protocol can be scaled up to gram quantities under an exceptionally low catalyst loading (S/C = 40 000), and the resulting hydrogenation product can be further transformed into novel chiral ligands that show promise in asymmetric catalysis.

Introduction

The asymmetric hydrogenation of carbonyl compounds stands as a pivotal methodology in fine chemical and pharmaceutical synthesis. Early catalytic systems predominantly followed inner-sphere mechanisms, showing modest efficiency.[1] This model shifted with the introduction of Noyori-type HM–NH bifunctional catalysts, which revolutionized the field through their outer-sphere mechanism, achieving unprecedented levels of enantiocontrol and catalytic turnover.[2] Mechanistic studies have established that these catalysts engage the substrate through cooperative metal–hydride (M–H) and N–H functionalities, enabling a concerted hydrogen transfer *via* hydrogen bonding (Scheme 1A).[3] Since then, asymmetric hydrogenation catalysts developed by numerous scientists worldwide, such as Zhou,[4] Zhang,[5] Morris,[6] Clarke,[7] Beller[8] and others,[9] have largely followed this model.

With the continuous advancement of asymmetric hydrogenation, the design of more efficient catalysts has become crucial for achieving higher activity and efficiency. Compared to neutral catalysts, anionic metal complexes-bearing formal negative charges-can increase the electronegativity of metal-bound hydride atoms,[10] potentially enhancing catalytic performance. The use of anionic catalysts in homogeneous hydrogenation dates back to the 1980s, when Pez and colleagues demonstrated their unique advantages.[11] Since then, the concept of anionic catalysis has been successfully applied to other catalytic transformations.[12] These developments have inspired efforts to incorporate anionic motifs into the established MH–NH system, to exploit their inherent reactivity advantages. In 2001, it was reported that the addition of excess base plays a crucial role in maintaining the high activity of Noyori-type catalysts,[13] leading to the proposal of a more efficient HM–NM′ model in which a deprotonated amino group (N–M′) operates in concert with a metal hydride (M–H).[14] Density functional theory (DFT) calculations support this mechanism, illustrating a stepwise hydrogen transfer process wherein the rate-determining transition state is stabilized by noncovalent interactions (Scheme 1A).[14] Further evidence for the involvement of such anionic species comes from the structural and spectroscopic characterization of alkali metal–hydride–amidate complexes, demonstrating their existence and potential role as active intermediates.[15] Beyond the extensively studied HM–NM′

[a] *State Key Laboratory of Green Chemical Synthesis and Conversion, College of Pharmaceutical Sciences, Zhejiang University of Technology, Hangzhou, 310014, P. R. China. E-mail: lingfei@zjut.edu.cn; weihuizhong@zjut.edu.cn*

[b] *School of Chemistry and Chemical Engineering, Shandong University, Jinan, 250100, People's Republic of China. E-mail: hujy2023@163.com*

[c] *Huzhou Key Laboratory of Medical and Environmental Applications Technologies, School of Life Sciences, Huzhou University, Huzhou, 313000, P. R. China*
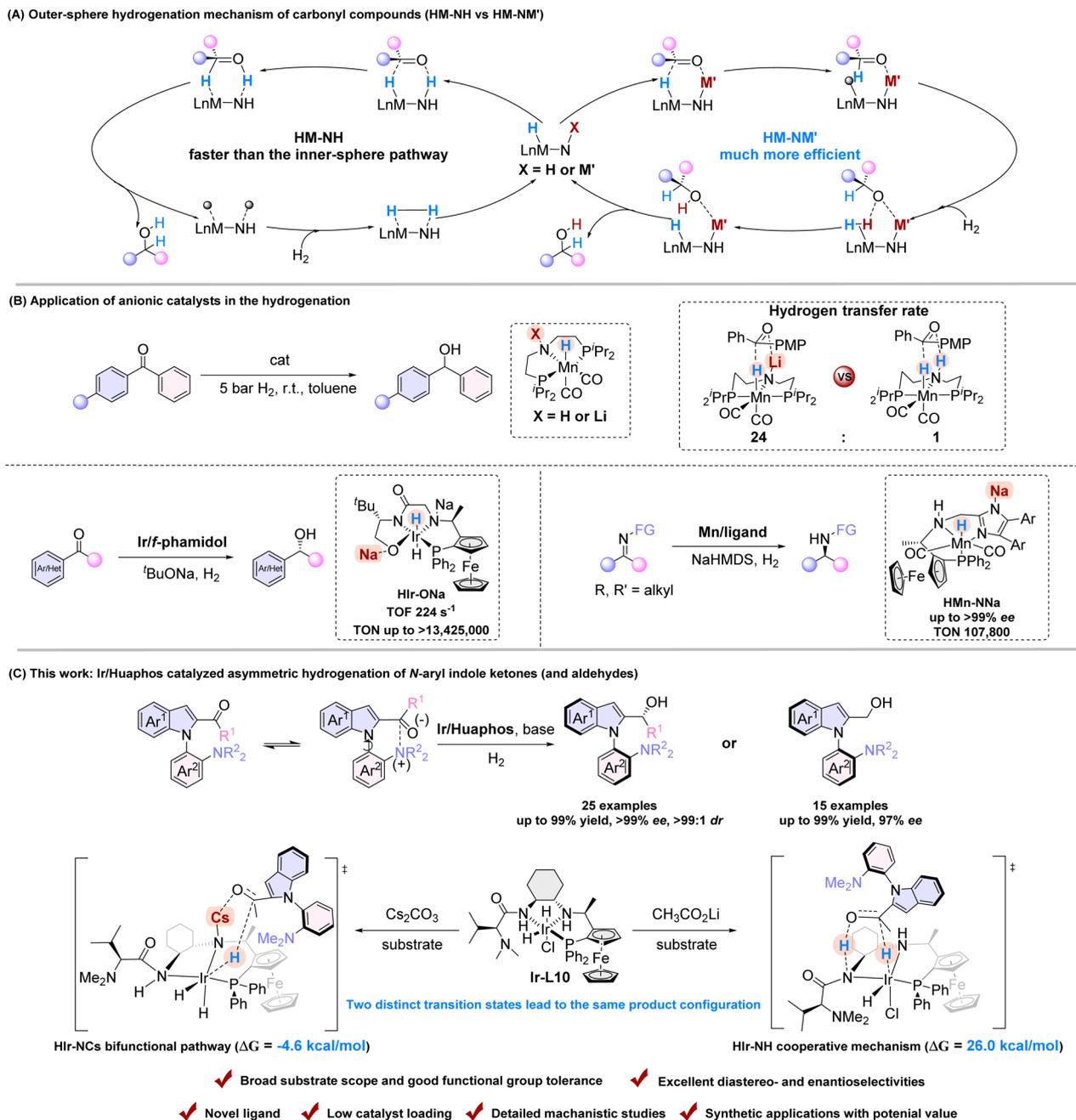
Scheme 1 (A) Outer-sphere hydrogenation mechanism of carbonyl compounds; (B) previous reports; (C) this work.

class of catalysts, Poli *et al.* reported on iridium systems that, although not deprotonated, still exhibit behavior consistent with anionic catalysis, likely because strong bases generate transient anionic species. Their work underscores the broader relevance of anionic pathways and the critical role of strong bases in enabling high catalytic efficiency.[16] Additional implementations of the MH–NM′ system have since been documented, underscoring its general utility in catalytic hydrogenation.[17]

In 2022, Liu[17a] first synthesized and characterized a lithium manganese hydride amidate complex (HMn–NLi). Kinetic studies and DFT calculations revealed that HMn–NLi reacts

with ketones 24-fold faster than its parent amino hydride (HMn–NH), due to the significantly stronger affinity between the N–Li moiety and carbonyl groups compared to the N–H group, demonstrating the superiority of metal-assisted hydrogen transfer (Scheme 1B). In 2023, Zhang[17b] combined the concept of anionic catalysts with multidentate ligands to develop a class of tetradentate anionic iridium catalysts exhibiting exceptional efficiency in the asymmetric hydrogenation of ketones (TOF = 224 s^{-1}, TON up to 13 425 000, Scheme 1B). Liu and colleagues[17c] extended anionic catalysis to chiral manganese systems, enabling the asymmetric hydrogenation of dialkyl ketimines (Scheme 1B). Comprehensive structural and

mechanistic studies confirmed that both catalyst architecture and cation participation enhance enantioselectivity. These examples highlight the superior performance of catalysts based on the HM–NM′ model. However, its application has so far been largely restricted to systems involving small alkali metal cations, and in asymmetric hydrogenation, it remains primarily limited to the construction of central chirality, with very few reports on the synthesis of axially chiral compounds.

Axial chirality represents an important class of molecular frameworks that are widely present in natural products, pharmaceuticals, functional materials, bioactive molecules, as well as privileged chiral ligands and organocatalysts.[18] As a result, significant efforts have been made over the past two decades to develop efficient strategies for constructing axial chirality.[19] However, to date, only a few examples[20] have employed asymmetric hydrogenation for the construction of axially chiral compounds. Despite these reports, challenges remain, including limited substrate scope, suboptimal stereoselectivity, high catalyst loading, and poorly defined catalyst properties.

In response to these challenges, we herein report a novel class of chiral ligands (**Huaphos**) building on our previous work in ligand design,[21] which were successfully used in iridium-catalyzed asymmetric hydrogenation of configurationally labile *N*-aryl indole ketones (and aldehydes), affording excellent stereoselectivities (up to >99% ee, >99 : 1 dr). Spectroscopic analysis revealed that the neutral **Ir/Huaphos** complex (**HIr-NH**) is activated by cesium carbonate to generate a novel anionic iridium catalyst (**HIr-NCs**). DFT calculations further indicate that the large cesium cation engages in a significant electrostatic interaction with the oxygen atom of the substrate, which substantially lowers the activation barrier and accelerates the reaction rate. This cation–substrate interaction, enabled by the bulky Cs^+, represents a key design element for achieving high efficiency. With the aid of anionic iridium catalyst (**HIr-NCs**), this protocol can be scaled up to gram quantities using a low catalyst loading (S/C = 40 000). The resulting hydrogenation products can be further transformed into novel chiral ligands, which show promising applications in asymmetric catalysis.

Results and discussion

Reaction optimization

The chiral **Huaphos** ligands can be readily synthesized using well-established methods in 50–75% yields (SI, Page S1). With the ligands in hand, we proceeded to investigate their application in the asymmetric hydrogenation of *N*-aryl indole ketones.

In the initial study, 1-(1-(2-(dimethylamino)phenyl)-1*H*-indol-2-yl) ethan-1-one (**1a**) was chosen as the model substrate, with ^{t}BuOLi as the base and ^{i}PrOH as the solvent to evaluate a series of catalytic systems. We first tested the efficacy of Ir/*f*-diaphos that had demonstrated exceptional results in the asymmetric hydrogenation of simple ketones. Disappointedly, it delivered only low yield and poor stereoselectivity (Table 1 entries 1 and 2). Subsequently, the new catalytic system was evaluated under identical conditions, affording the desired product in moderate yield and stereoselectivity. To explore the substituent effects on catalytic performance, a series of amino

acid-derived ligands were systematically assessed. Among them, **L10** proved optimal, providing the highest yield and stereoselectivity (entries 3–10). Following a systematic screening of solvents and bases, Cs_2CO_3 and toluene were identified as the optimal system, providing the highest stereoselectivity (>99% ee, >99 : 1 dr) and fastest reaction rate (complete in 12 h). Although CH_3CO_2Li delivered comparable stereoselectivity (with CH_3CO_2Na and CH_3CO_2Cs showing slightly lower selectivity), the transformation required 36 hours to reach full conversion (entries 11–15 and SI, Pages S18, S19, Tables S1 and S2). Moreover, the inclusion of one equivalent of 21-crown-7 as a cesium cation sequestering agent led to a significant decrease in conversion. The above results suggest that CH_3CO_2Li (a weak base) and Cs_2CO_3 (a strong base) may play distinct roles in the reaction. As a result, the optimal reaction conditions were identified as follows: [Ir(COD)Cl]$_2$/**L10** (0.1 mol%) as catalyst,

Table 1 Optimization of reaction conditions^a
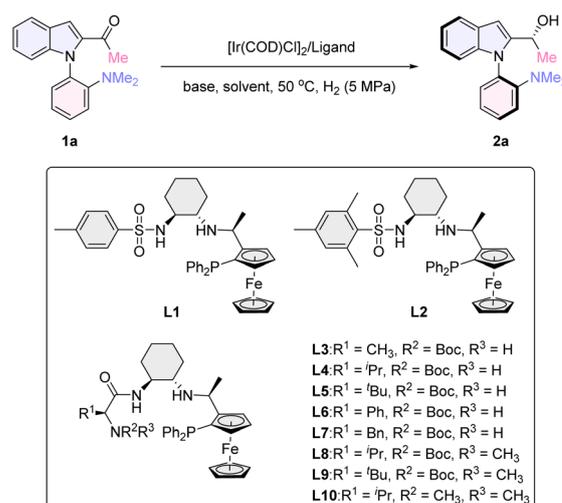
Entry	Ligands	Bases	Solvents	Conv. (%)	ee (%)	dr
1	**L1**	^{t}BuOLi	^{i}PrOH	10	20	1 : 1
2	**L2**	^{t}BuOLi	^{i}PrOH	15	28	1 : 1
3	**L3**	^{t}BuOLi	^{i}PrOH	50	52	4 : 1
4	**L4**	^{t}BuOLi	^{i}PrOH	60	58	17 : 3
5	**L5**	^{t}BuOLi	^{i}PrOH	55	56	4 : 1
6	**L6**	^{t}BuOLi	^{i}PrOH	58	53	4 : 1
7	**L7**	^{t}BuOLi	^{i}PrOH	57	50	5 : 1
8	**L8**	^{t}BuOLi	^{i}PrOH	55	58	9 : 1
9	**L9**	^{t}BuOLi	^{i}PrOH	50	56	9 : 1
10	**L10**	^{t}BuOLi	^{i}PrOH	70	65	20 : 1
11	**L10**	^{t}BuOLi	EA	80	78	20 : 1
12	**L10**	^{t}BuOLi	THF	78	76	9 : 1
13	**L10**	^{t}BuOLi	Toluene	86	82	20 : 1
14^b	**L10**	CH_3CO_2Li	Toluene	99	>99	>99 : 1
15	**L10**	**Cs_2CO_3**	**Toluene**	99	>99	>99 : 1
16^c	**L10**	Cs_2CO_3	Toluene	15	85	20 : 1

^{a} Reaction conditions: **1a** (0.25 mmol), [Ir(COD)Cl]$_2$ (0.05 mol%), ligand (0.11 mol%), base (10 mol%), solvent (1 mL), 50 °C, H$_2$ (5 MPa) and 12 h. The conversion was determined by GC analysis. The ee and dr values were determined by HPLC analysis. ^{b} 36 h. ^{c} 21-Crown-7 (0.25 mmol) was used as the additive.

Cs$_2$CO$_3$ (10 mol%) as base, toluene as solvent, under 5 MPa H$_2$ at 50 °C.

Substrate scope

With the optimized conditions established, the substrate scope of the iridium-catalyzed dynamic kinetic resolution (DKR) of ketones for the construction of C–N axial chirality was explored (Scheme 2). To elucidate the distinct roles of Cs$_2$CO$_3$ and CH$_3$-CO$_2$Li in the reaction, both bases were evaluated under otherwise identical conditions. We initially investigated a series of N-aryl indole ketones bearing substituents at various positions on the indole and benzene rings. Nearly all substrates delivered the corresponding products (**2a–2o**) with excellent enantioselectivity (>99% ee) and diastereoselectivity (>99 : 1 dr).

Notably, substrates bearing electron-withdrawing groups (**1d, 1f–1h, 1k**) exhibited significantly faster reaction rates compared to those with electron-donating groups (**1b, 1c, 1e, 1i, 1j, 1l–1o**), suggesting a beneficial electronic effect on the reaction kinetics. The absolute configuration of this class of products was unambiguously determined for the first time through X-ray crystallographic analysis of compound **2g**. Comparative studies revealed that reactions employing Cs$_2$CO$_3$ as base proceeded significantly faster than those with CH$_3$CO$_2$Li, while maintaining comparable stereoselectivity. Notably, when Cs$_2$CO$_3$ was employed as the base, the 3-methyl-substituted substrate **1b** was efficiently converted to **2b**, whereas CH$_3$CO$_2$-Li afforded only low yield under identical conditions. Next, we evaluated aliphatic acyl and diaryl substrates (**1p–1w**) under the
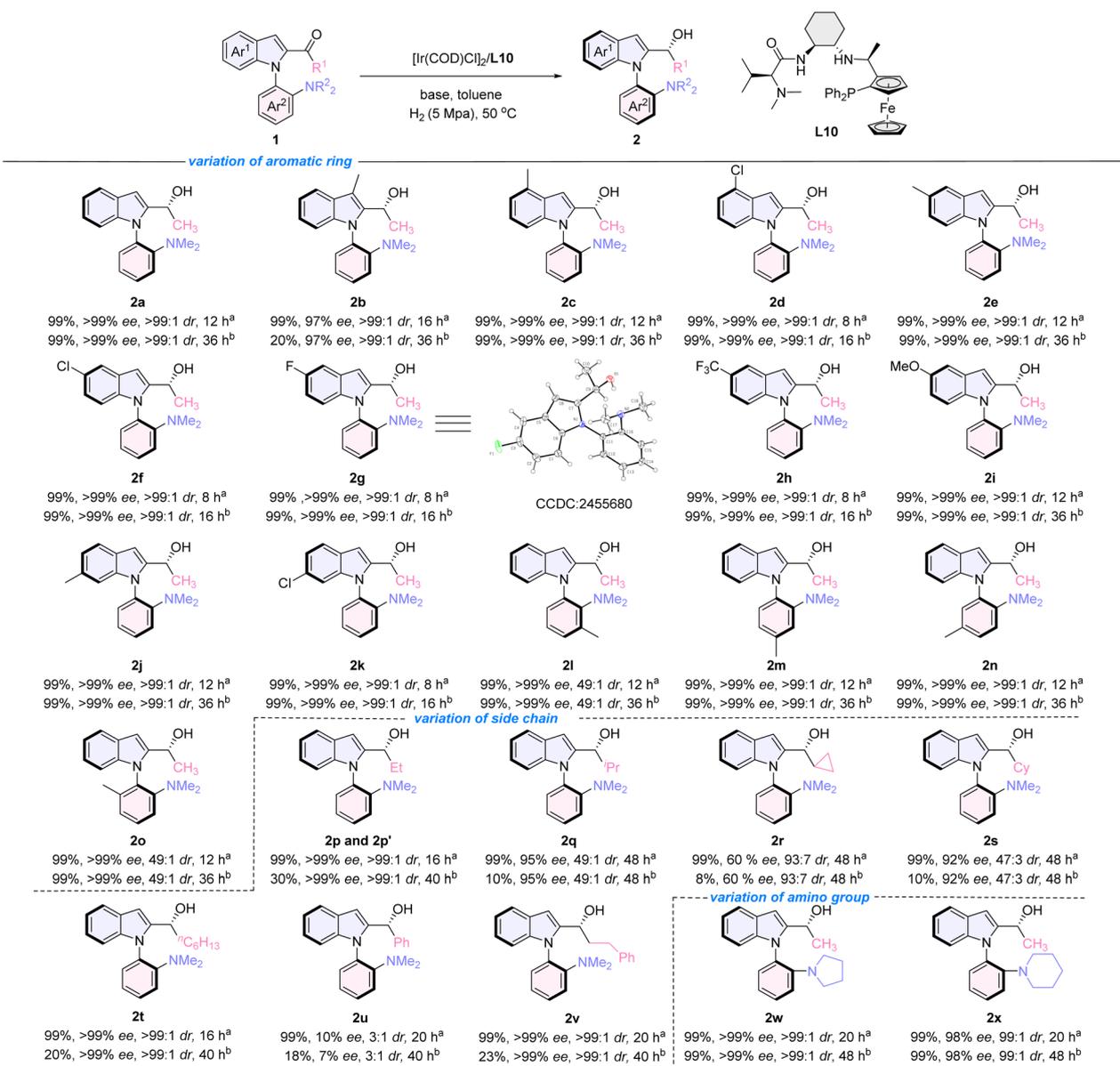
Scheme 2 Substrate scope of N-aryl indole ketones. [a]Reaction conditions: **1** (0.25 mmol), [Ir(COD)Cl]$_2$ (0.05 mol%), **L10** (0.11 mol%), Cs$_2$CO$_3$ (10 mol%), toluene (1 mL), 50 °C and H$_2$ (5 MPa). Isolated yields were obtained by flash chromatography and the ee and dr values were determined by HPLC analysis. [b]CH$_3$CO$_2$Li was used as the base instead of Cs$_2$CO$_3$.

standard conditions. Similar to the results observed with **1b**, these substrates showed low conversion rates when CH_3CO_2Li was used as the base. After replacing the base with Cs_2CO_3, complete conversion was achieved for substrates **1p–1w**. The corresponding hydrogenation products were obtained with high stereoselectivity: **2p** (>99% ee, >99 : 1 dr), **2q** (95% ee, 49 : 1 dr), and **2s** (92% ee, 47 : 3 dr). Interestingly, during the hydrogenation of substrates containing a vinyl substituent (SI, Page S15, substrate **1y**), the terminal C=C bond was also completely reduced, leading to the formation of the desired product **2p′** in similar yield and stereoselectivity. This unexpected observation reveals the robustness of the catalytic system and suggests new opportunities for the **Huaphos** ligand in broader catalytic transformations. However, the cyclopropyl-substituted product (**2r**) showed reduced stereoselectivity (60% ee, 93 : 7 dr), likely due to the inherent rigidity of the three-membered ring system. Substrate bearing an *n*-hexyl group was also successfully transformed into the corresponding product (**2t**) with up to >99% ee, >99 : 1 dr. Replacing the alkyl group with a phenyl group (**2u**), led to a sharp drop in enantioselectivity to 10% ee (3 : 1 dr), presumably due to restricted rotation and increased steric congestion from the aromatic ring. To address this limitation, we introduced a two-carbon spacer between the phenyl ring and the carbonyl group prior to hydrogenation. As expected, this structural modification restored both high yield and excellent stereoselectivity in the resulting product (**2v**). Finally, substrates derived from cyclopentylamine and cyclohexylamine were also compatible, delivering **2w** (>99% ee, >99 : 1 dr) and **2x** (98% ee, 99 : 1 dr), respectively, regardless of the base used. These results collectively demonstrate the broad applicability and versatility of the **Ir/Huaphos** catalytic system in constructing C–N axially chiral architectures.

Synthetic application

To demonstrate the practicality of the developed strategy, a gram-scale hydrogenation of **1a** (2.78 g) was performed under 5 MPa of H_2 at 50 °C, using a low catalyst loading (S/C = 40 000) for 30 hours to afford the corresponding product **2a** with up to >99% ee and >99 : 1 dr (Scheme 3A). The hydroxyl group in **2a** was then converted into an amino group with inversion of configuration *via* a classic Mitsunobu reaction[22] yielding chiral amine **3a** (Scheme 3B). Chiral amines serve as valuable synthetic building blocks, enabling the efficient synthesis of a wide range of chiral ligand architectures.[23] For example, **3a** was condensed with 3,5-bis(trifluoromethyl)phenyl isothiocyanate to afford a novel bifunctional thiourea catalyst **4a** in 90% yield and 95% ee (Scheme 3C). In addition, chiral amine **3a** could be further transformed into chiral P/N ligands **5a** and **6a** through amide condensation and reductive amination respectively (Scheme 3D and E). The chiral P/N ligand frameworks exhibit remarkable versatility in asymmetric transformations.[24] Notably, the bidentate ligand **6a** was successfully applied in the asymmetric hydrogenation of acetophenone, affording the secondary alcohol product **7a** with 77% ee (Scheme 3F). This application underscores the synthetic value and promising potential of the ligand architecture derived from this catalytic DKR strategy. Furthermore, we conducted a preliminary investigation into the catalytic performance of **4a** in asymmetric transformations (SI, Page S36).

Mechanistic studies

As reported in the literature,[19j] a weak Lewis acid–base interaction exists between the carbonyl group of the analogous aldehyde substrate and the adjacent NMe_2 moiety, facilitating rotation around the C–N bond through a six-membered cyclic
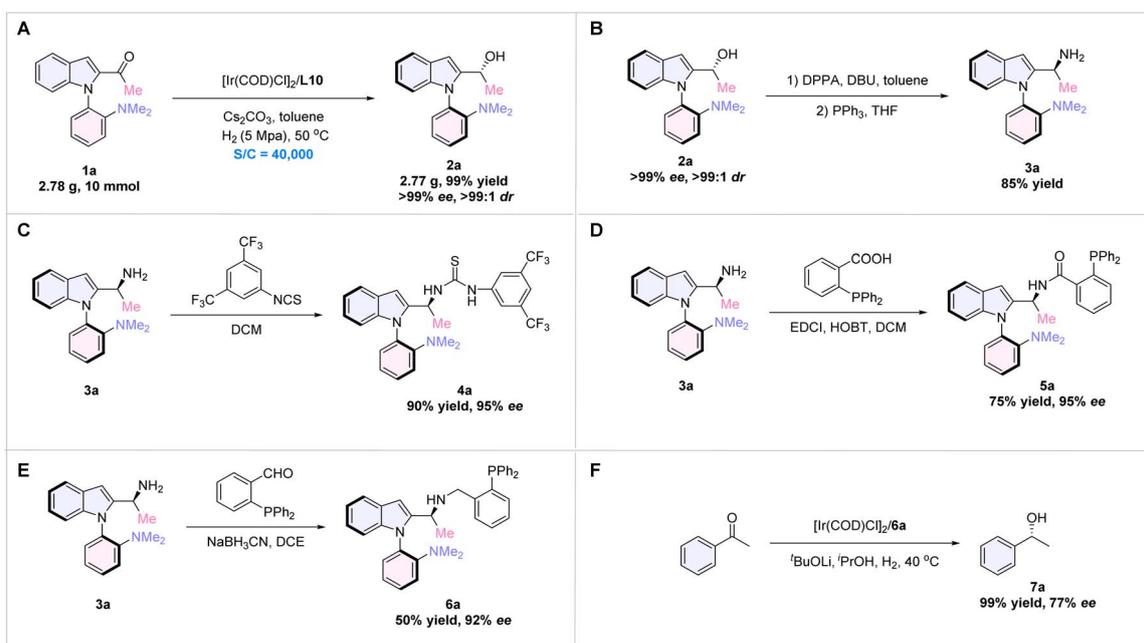

Scheme 3 Gram scale synthesis of **2a** and its transformations.

transition state. This conformational lability enables rapid racemization, fulfilling a key requirement for an effective dynamic kinetic resolution (DKR) process-fast substrate racemization under the reaction conditions. This mechanistic rationale is further supported by DFT calculations. To experimentally validate this hypothesis, we first investigated the configurational stability of the C–N axial chirality through racemization studies. When compound **2a** was stirred in toluene at 80 °C for 12 hours, chiral HPLC analysis revealed no discernible erosion of enantiomeric excess, indicating high stereochemical stability under these conditions (Scheme 4A, SI for details, Page S37). Then control experiments were performed. Notably, oxidation of the hydroxyl group in **2a** to the corresponding ketone led to complete racemization of the axial chirality (Scheme 4B), consistent with the proposed mechanism. Subsequent DFT calculations of the rotational barriers for **1a** and **2a** revealed that **1a** has a significantly lower barrier (25.8 kcal mol^{-1}) compared to **2a** (36.6 kcal mol^{-1}). This substantial difference further supports the role of the carbonyl group in reducing rotational energy and facilitating racemization, thus corroborating the proposed DKR mechanism (SI, Page S67).

Informed by previous studies,[15,17] we performed a comprehensive characterization of the catalyst to better understand the nature of the active catalytic species. First, the **Ir-L10** complex was thoroughly characterized using a combination of spectroscopic and analytical techniques. The neutral **Ir-L10** complex was prepared by reacting ligand **L10** with [Ir(COD)Cl]$_2$ under an H$_2$ atmosphere. In the ^{1}H NMR spectrum, two new downfield-shifted resonances were observed at δ 8.40 ppm and δ 8.05 ppm (Scheme 4D, SI, Page S42), which were assigned to the amide N–H and amino N–H protons, respectively, upon coordination to the iridium center. This significant deshielding indicates a strong electronic interaction between the nitrogen lone pairs and the metal, consistent with successful formation of the Ir–N bonds. Furthermore, ATR-IR spectroscopy provided compelling evidence for coordination: the N–H stretching vibrations of the amide (from 3454 to 3418 cm^{-1}) and amino groups (from 3381 to 3257 cm^{-1}) shifted to lower wavenumbers, while the carbonyl (C=O) stretch shifted to higher wavenumbers (from 1711 to 1739 cm^{-1}, SI, Page S41). The ^{31}P NMR spectrum showed a significant downfield shift of the phosphorus resonance from δ −25.0 ppm in the free ligand **L10** to δ 7.2 ppm in the **Ir-L10** complex, providing strong evidence for coordination of the phosphine moiety to the iridium center (Scheme 4D and SI, Page S43). Additionally, two distinct hydride resonances were observed at δ −21.0 ppm and −28.0 ppm in the ^{1}H NMR spectrum, characteristic of chemically inequivalent Ir–H ligands in an octahedral Ir(III) complex (Scheme 4D and SI, Page S43). These signals were further corroborated by ATR-IR spectroscopy, which revealed two sharp bands at 2194 cm^{-1} and 2146 cm^{-1}, consistent with terminal Ir–H stretching vibrations. Together, these data confirm the presence of two hydride ligands bound to the iridium center. Finally, HRMS confirmed the molecular formula of **Ir-L10**, detecting the [M–H]$^-$ ion at m/z 866.2281 (calcd 866.2280, SI, Page S39). Taken together with NMR and ATR-IR data, this result unambiguously
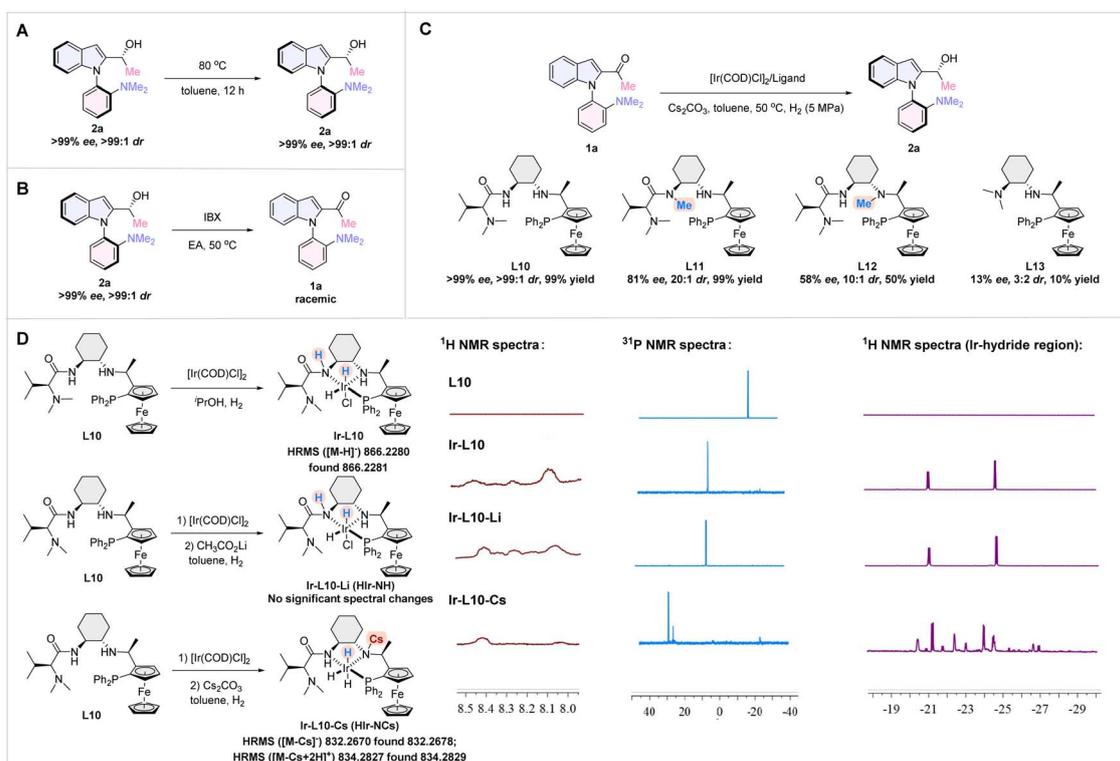
Scheme 4 Control experiment and spectroscopic characterization of the catalyst.

establishes **Ir-L10** as a neutral, tridentate PNN-coordinated iridium(III) complex.

Subsequent mixing of **L10**, [Ir(COD)Cl]$_2$ and CH$_3$CO$_2$Li under a hydrogen atmosphere showed no observable changes in its spectroscopic characteristics (Scheme 4D and SI, Pages S44–S46). In contrast to CH$_3$CO$_2$Li, treatment with Cs$_2$CO$_3$ induced significant spectroscopic changes in the iridium complex. The ^{1}H NMR spectrum showed nearly complete disappearance of the resonance at δ 8.05 ppm (assigned to the amino N–H proton), indicating deprotonation of the coordinated amine (Scheme 4D and SI, Page S54). Concurrently, the ^{31}P NMR signal shifted dramatically from δ 7.2 ppm (in the neutral complex) to δ 31.5 ppm (Scheme 4D and SI, Page S55), likely reflecting structural reorganization induced by the deprotonation

process. ATR-IR analysis further revealed a new Ir–H stretching vibration, suggesting the formation of a third Ir–H ligand (SI, Page S55), due to chloride dissociation under basic conditions and subsequent hydrogenation under H$_2$. HRMS confirmed the formation of two key species: the [M–Cs]$^-$ ion at m/z 832.2678 and the [M–Cs + 2H]$^+$ ion at m/z 834.2829 (SI, Page S53). These data collectively support the formation of an anionic, tridentate coordinated iridium(III) species (**Ir-L10-Cs**) which serves as a key activated catalyst in the reaction. In addition, we sought to characterize the transformation of the catalyst under the influence of Cs$_2$CO$_3$. Comprehensive spectroscopic analysis by NMR, HRMS, and ATR-IR (SI, Pages S47–S55) supports a mechanistic pathway in which the catalyst undergoes simultaneous departure of the amide N–H proton and chloride ligand,
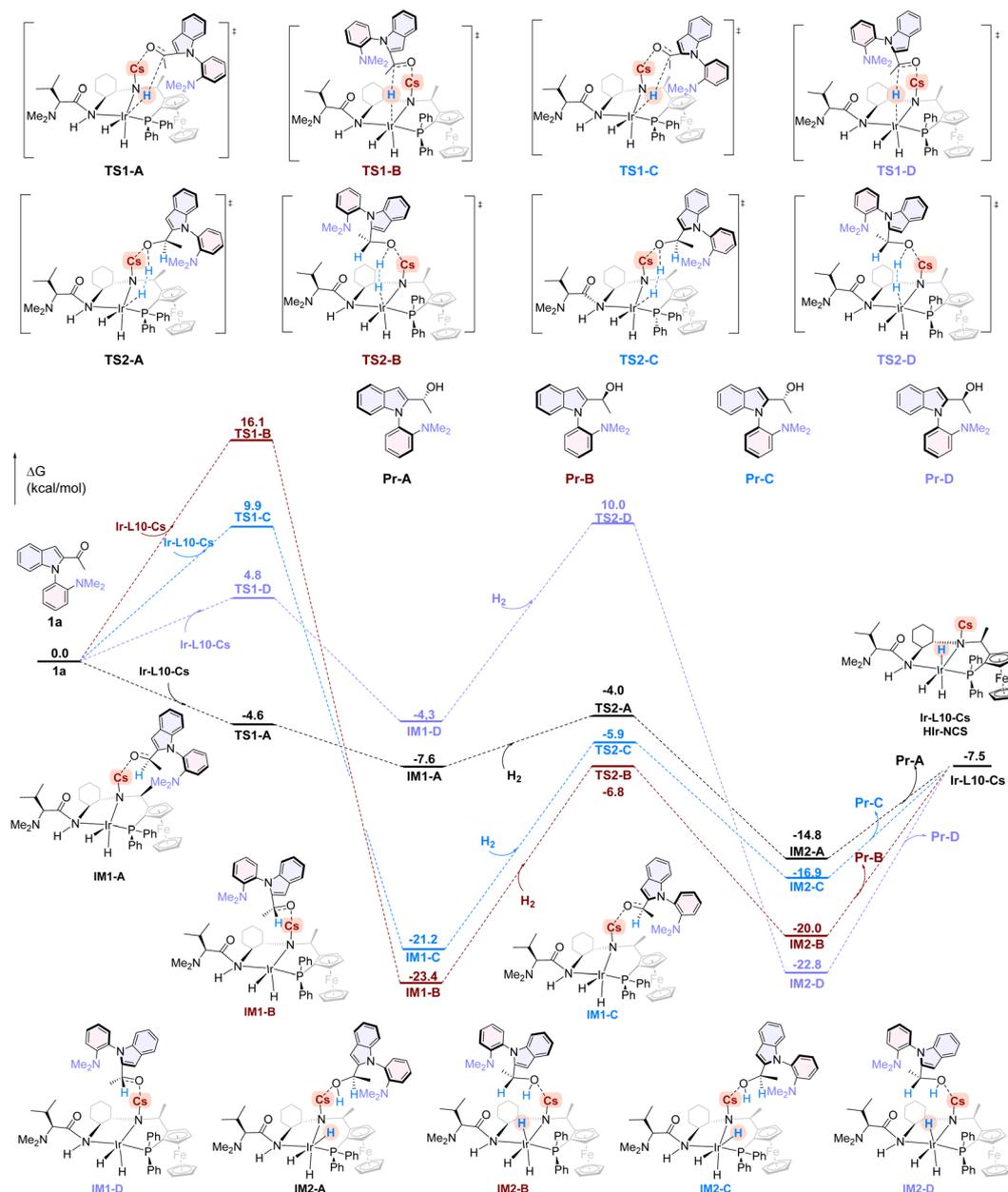

Fig. 1 DFT studies on the cesium cation promoted asymmetric hydrogenation process.

deprotonation of the amino N–H group, and oxidative addition of H_2, ultimately forming an anionic active species.

To validate the proposed anionic catalyst model, we synthesized structurally modified versions of ligand **L10** and evaluated their performance under standard reaction conditions employing Cs_2CO_3 as base. The amide N–H methylated ligand **L11** exhibited modestly reduced enantioselectivity, while the amine N–H methylated ligand **L12** showed significantly diminished reactivity and enantioselectivity (Scheme 4C). This stark contrast underscores the critical role of the amine N–H group in catalyst activation, providing strong support for the formation of the deprotonated anionic **Ir-L10-Cs** species as the active catalyst. Moreover, the results from **L13** demonstrate that the amino acid moiety plays a significant role in the ligand. The origin of the significant difference in catalytic performance between *f*-diaphos and **Huaphos** remains under investigation.

In light of previous literature,[16,17b,c] we propose that the anionic **Ir-L10-Cs** (**HIr-NCs**) and neutral **Ir-L10** (**HIr-NH**) catalysts operate *via* distinct mechanistic pathways-a hypothesis supported by DFT calculations. For the hydrogenation mechanism of **Ir-L10-Cs**, as illustrated in Fig. 1, the entire process is divided into two stages. In Stage 1, reactant first undergoes hydrogenation at the carbonyl carbon through transition state **TS1**, a key step that simultaneously establishes both axial chirality and the stereogenic center at the carbonyl carbon, thereby determining the overall stereoselectivity. The relative energy barriers for **TS1-A** (-4.6 kcal mol^{-1}), **TS1-B** (4.8 kcal mol^{-1}), **TS1-C** (9.9 kcal mol^{-1}), and **TS1-D** (16.1 kcal mol^{-1}) govern the preferential formation of **Pr-A** as the major product. Moreover, the energy differences among these transition states are consistent with the experimental observed enantiomeric excess (>99% ee) and diastereomeric ratio (>99 : 1 dr). In Stage 2, molecular hydrogen adds to the **IM1** intermediate *via* **TS2**, in which one hydrogen atom from H_2 is transferred to the carbonyl oxygen of the substrate, while the other binds to the iridium center. This leads to the formation of **IM2**, which subsequently releases the final products (**Pr-A**, **Pr-B**, **Pr-C**, and **Pr-D**) upon catalyst regeneration. To enhance computational efficiency, the simplified model neglects interactions between solvent and cations,[14,17b] as well as the potential effects of carbonate/bicarbonate ions, the latter being particularly challenging to describe accurately with conventional Gaussian-type DFT methods. Importantly, weak π-interactions between toluene and metal ions may occur under actual reaction conditions, potentially modulating conformational equilibria and consequently shifting the activation barriers (SI for details, Pages S67 and S68). A more sophisticated modeling strategy, such as that employed by Poli *et al.*,[16] would better account for these subtle yet non-negligible factors. In addition, density functional theory (DFT) calculations were performed to investigate the hydrogenation pathway mediated by the neutral **Ir-L10** catalyst (SI, Page S66). In this pathway, hydrogen transfer occurs in a single step *via* a concerted, bifunctional mechanism: the hydride on iridium attacks the carbonyl carbon, while the amide N–H proton is delivered to the carbonyl oxygen. Although repeated attempts failed to locate a well-defined transition state that fully accounts for the enantioselectivity in the
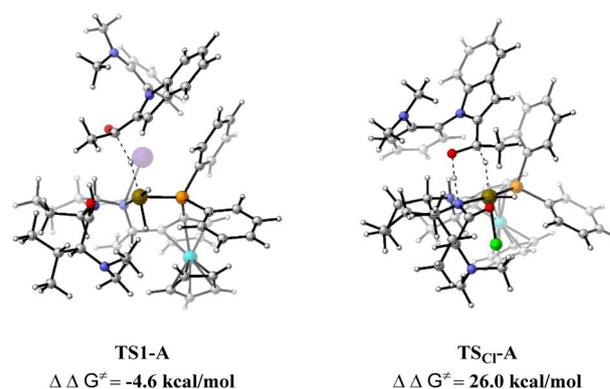

TS1-A
$\Delta\Delta G^{\neq} = -4.6$ kcal/mol

TS$_{Cl}$-A
$\Delta\Delta G^{\neq} = 26.0$ kcal/mol

Fig. 2 Reaction energy barriers: anionic *vs.* neutral catalytic systems.

hydrogenation process (SI for details, Pages S65 and S66), it is noteworthy that the significant energy difference between **Ir-L10-Cs** and **Ir-L10** inherently reflects the substantial advantage of the anionic catalytic system (Fig. 2). This difference is primarily attributed to the strong electrostatic interaction between the Cs^+ cation in **Ir-L10-Cs** and the carbonyl oxygen of substrate **1a**, which stabilizes the transition state and lowers the activation energy. These results indicate that **Ir-L10-Cs** exhibits substantially enhanced hydrogenation activity compared to **Ir-L10**, in excellent agreement with experimental observations. Integrated analysis of experimental results, spectroscopic data, and DFT calculations leads to a comprehensive catalytic cycle for the hydrogenation under varying basic conditions (Scheme 5). Rapid C–N bond rotation, mediated by a six-membered pericyclic transition state, facilitates dynamic racemization of the substrate. In this framework, the *S*-configured isomer is selectively activated and reduced by either the anionic **Ir-L10-Cs** catalyst or the neutral **Ir-L10** species, leading to product formation.

Strategy extension

Having successfully accomplished the dynamic kinetic resolution (DKR) of *N*-aryl indole ketones, we hypothesized that the Ir-catalyzed asymmetric hydrogenation system might also be applicable to *N*-aryl indole aldehydes. Surprisingly, the optimal ligand for the reaction shifted from **L10** to **L9**. After brief optimization of the reaction parameters (SI for details, Pages S27 and S28), the **Ir-L9** catalytic system was applied to a series of aldehyde substrates, yielding the corresponding products with moderate to excellent enantioselectivity (Scheme 6). Condition screening revealed a trade-off between reaction rate and stereoselectivity: while Cs_2CO_3 promoted faster conversion, reactions employing CH_3CO_2Li delivered slightly higher enantioselectivity. On this basis, CH_3CO_2Li was selected as the optimal base for maximizing ee. Consistent with the trend observed for ketones, aldehydes bearing electron-withdrawing groups (**9d**, **9f–9h**, **9k**) reacted significantly faster than those with electron-donating substituents (**9b**, **9c**, **9e**, **9i**, **9j**, **9l–9o**). In contrast, the latter group generally afforded higher enantiomeric excess, suggesting that electronic effects influence enantioselectivity differently than reaction kinetics.
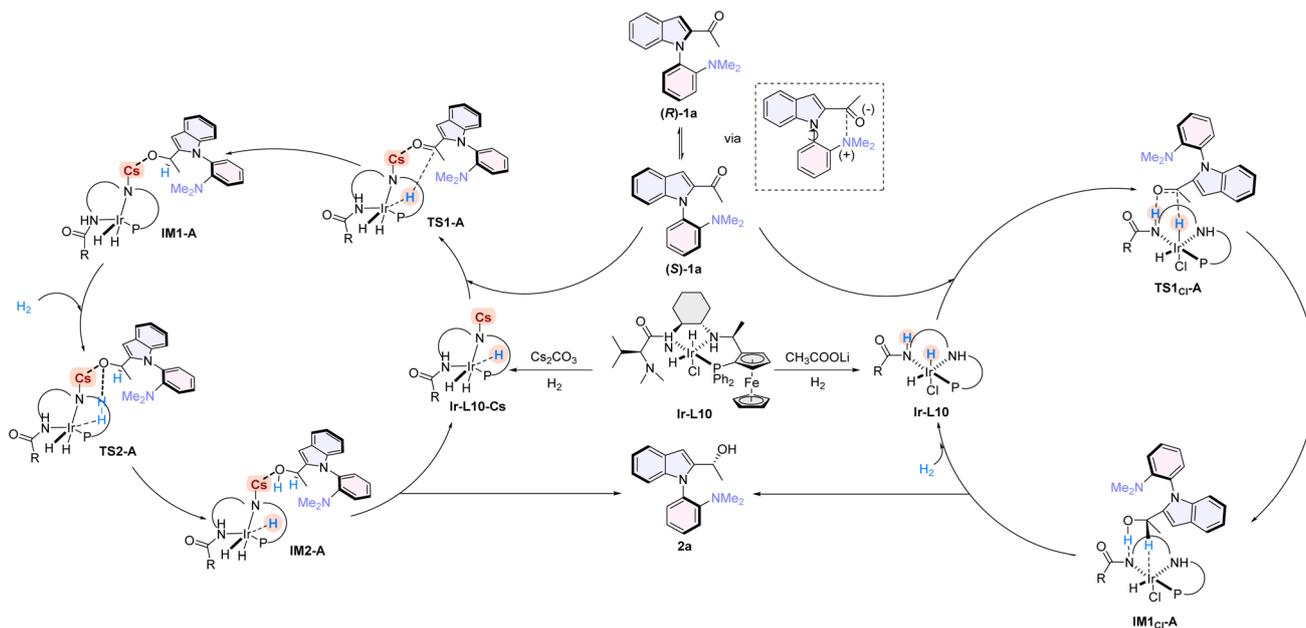
Scheme 5 Proposal catalytic cycle for AH under Cs$_2$CO$_3$ or CH$_3$CO$_2$Li.
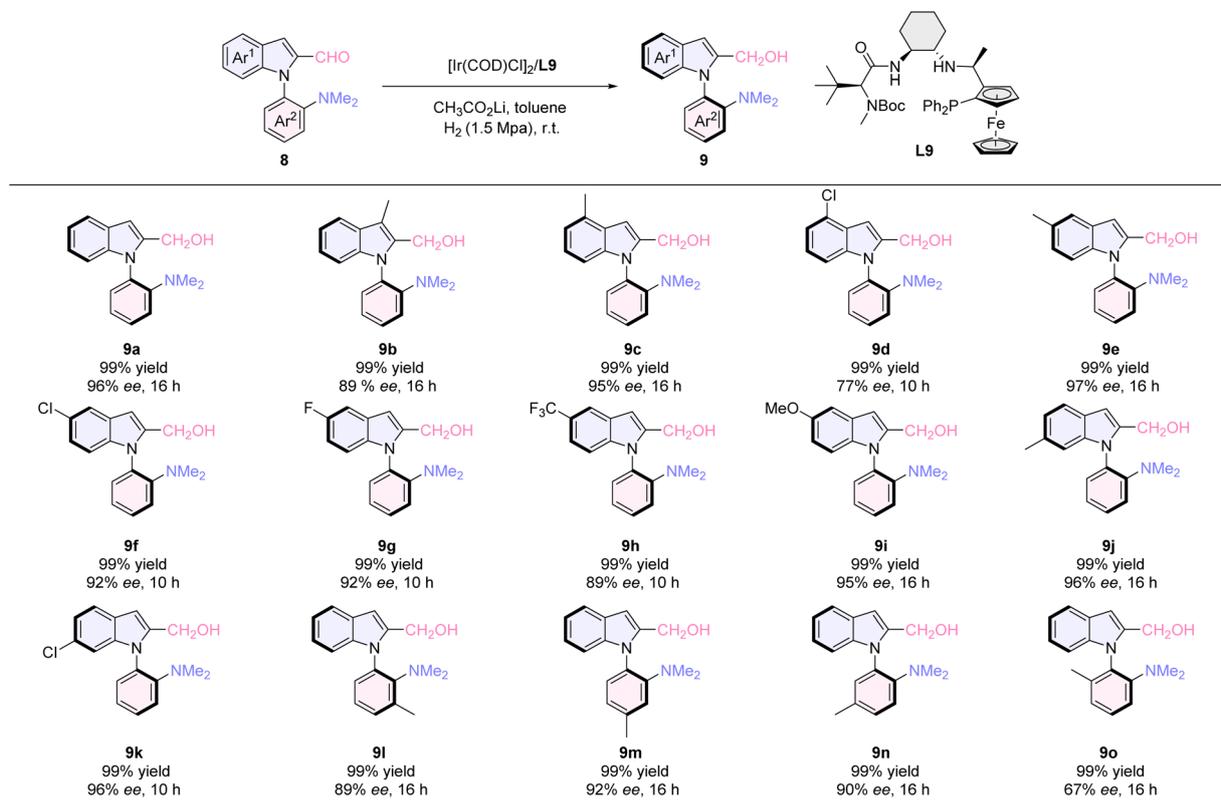
Scheme 6 Substrate scope of *N*-aryl indole aldehydes. Reaction conditions: **8** (0.25 mmol), [Ir(COD)Cl]$_2$ (0.05 mol%), **L9** (0.11 mol%), CH$_3$CO$_2$Li (10 mol%), toluene (1 mL), r.t. and H$_2$ (1.5 MPa). Isolated yields were obtained by flash chromatography and the ee value was determined by HPLC analysis.

Unfortunately, compounds **9d** and **9o** showed lower ee values, despite their structural similarity to high-performing analogues. This may be attributed to steric hindrance that compromises effective chiral induction during the hydride transfer step. These results highlight the broad substrate scope and excellent stereocontrol achievable with this DKR strategy.

Finally, to elucidate the reaction pathway of *N*-aryl indole aldehydes, we characterized the catalyst **Ir-L9** (see the SI for details, Pages S56–S59). The results indicate that its structure is analogous to **Ir-L10**. Given that the hydrogenation of aldehydes also proceeds under catalysis by CH_3CO_2Li, we propose that the mechanism of **Ir-L9**-catalyzed aldehyde reduction is analogous to that of **Ir-L10**-mediated ketone hydrogenation.

Conclusions

In conclusion, we have developed a new class of chiral ferrocene-based tridentate ligands (**Huaphos**) which were used for Ir-catalyzed asymmetric hydrogenation of *N*-aryl indole ketones (and aldehydes) *via* a dynamic kinetic resolution process under neutral conditions, providing enantiomerically enriched *N*-aryl indole amino alcohols in high yields with excellent stereoselectivity (up to 99% yield, >99% ee, >99 : 1 dr). Under the influence of Cs_2CO_3, the **Ir/Huaphos** complex (**HIr-NH**) undergoes activation to form an anionic, tridentate iridium catalyst (**Ir-L10-Cs**), which exhibits significantly enhanced catalytic efficiency. The strong electrostatic interaction between the Cs^+ cation and the oxygen atom of the substrate effectively lower the reaction barrier, enabling rapid hydrogenation. The reaction can be conducted on a gram scale with a relatively low catalyst loading (S/C = 40 000) in the presence of **Ir-L10-Cs** (**HIr-NCs**), and reaction products can be readily transformed into novel chiral ligands, which exhibit promising applications in asymmetric catalysis. Research into the applications of this highly efficient catalyst and related products is still underway.

Author contributions

Xianghua Zhao: conceptualization, data curation, formal analysis, investigation, methodology, validation, visualization, writing – original draft, writing – review & editing; Xinyu Chen, Linxian Fan and Yulong Jiang: investigation and data curation. Yirui Chen and Dinguo Song: project administration. Junyuan Hu: resources, software (DFT calculations), visualization; Fei Ling and Weihui Zhong: funding acquisition, project administration, resources, supervision.

Conflicts of interest

There are no conflicts to declare.

Data availability

CCDC 2455680 contains the supplementary crystallographic data for this paper.[25]

All experimental procedures and data related to this study can be found in the supplementary information (SI). Supplementary information is available. See DOI: https://doi.org/10.1039/d5sc08462h.

Notes and references

1 S. E. Clapha, A. Hadzovic and R. H. Morris, *Coord. Chem. Rev.*, 2004, **248**, 2201–2237.

2 (*a*) T. Ohkuma, H. Ooka, S. Hashiguchi, T. Ikariya and R. Noyori, *J. Am. Chem. Soc.*, 1995, **117**, 2675–2676; (*b*) S. Hashiguchi and R. Noyori, *Acc. Chem. Res.*, 1997, **30**, 97–102; (*c*) T. Ohkuma, M. Koi-zumi, H. Doucet, T. Pham, M. Kozawa, K. Murata, E. Katayama, T. Yokozawa, T. Ikariya and R. Noyori, *J. Am. Chem. Soc.*, 1998, **120**, 13529–13530; (*d*) R. Noyori and T. Ohkuma, *Angew. Chem., Int. Ed.*, 2001, **40**, 40–73.

3 (*a*) K. J. Haack, S. Hashiguchi, A. Fujii, T. Ikariya and R. Noyori, *Angew. Chem., Int. Ed.*, 1997, **36**, 285–288; (*b*) M. Yamakawa, H. Ito and R. Noyori, *J. Am. Chem. Soc.*, 2000, **122**, 1466–1478; (*c*) K. A. Rashid, S. E. Clapham, A. Hadzovic, J. N. Harvey, A. J. Lough and R. H. Morris, *J. Am. Chem. Soc.*, 2002, **24**, 15104–15118; (*d*) R. Sandoval, T. Ohkuma, K. Muniz and R. Noyori, *J. Am. Chem. Soc.*, 2003, **125**, 13490–13503; (*e*) C. A. Sandoval, Y. Yamaguchi, T. Ohkuma, K. Kato and R. Noyori, *Magn. Reson. Chem.*, 2006, **44**, 66–75; (*f*) P. A. Dub and J. C. Gorden, *Nat. Rev. Chem.*, 2018, **2**, 396–408.

4 (*a*) J. H. Xie, X. Y. Liu, J. B. Xie, L. X. Wang and Q. L. Zhou, *Angew. Chem., Int. Ed.*, 2011, **50**, 7329–7332; (*b*) D. H. Bao, H. L. Wu, C. L. Liu, J. H. Xie and Q. L. Zhou, *Angew. Chem., Int. Ed.*, 2015, **54**, 8791–8794; (*c*) F. H. Zhang, C. Wang, J. H. Xie and Q. L. Zhou, *Adv. Synth. Catal.*, 2019, **361**, 2832–2835; (*d*) F.-H. Zhang, F.-J. Zhang, M.-L. Li, J.-H. Xie and Q.-L. Zhou, *Nat. Catal.*, 2020, **3**, 621–627.

5 (*a*) W. Wu, S. Liu, M. Duan, X. Tan, C. Chen, Y. Xie, Y. Lan, X. Dong and X. Zhang, *Org. Lett.*, 2016, **18**, 2938–2941; (*b*) L. Zeng, H. Yang, M. Zhao, J. Wen, J. H. R. Tucker and X. Zhang, *ACS Catal.*, 2020, **10**, 13794–13799; (*c*) J. Yu, F. Huang, W. Fang, C. Yin, C. Shi, Q. Lang, G.-Q. Chen and X. Zhang, *Green Synth. Catal.*, 2022, **3**, 175–178.

6 (*a*) A. A. Mikhailine, M. I. Maishan, A. J. Lough and R. H. Morris, *J. Am. Chem. Soc.*, 2012, **134**, 12266–12280; (*b*) W. Zuo, A. J. Lough, Y. Li and R. H. Morris, *Science*, 2013, **342**, 1080–1083; (*c*) P. O. Lagaditis, P. E. Sues, J. F. Sonnenberg, K. Y. Wan, A. J. Lough and R. H. Morris, *J. Am. Chem. Soc.*, 2014, **136**, 1367–1380.

7 M. B. Widegren, G. J. Harkness, A. M. Z. Slawin, D. B. Cordes and M. L. Clarke, *Angew. Chem., Int. Ed.*, 2017, **56**, 5825–5828.

8 (a) M. Garbe, Z. H. Wei, B. Tannert, A. Spannenberg, H. J. Jiao, S. Bacumann, M. Scalone, K. Junge and M. Beller, *Adv. Synth. Catal.*, 2019, **361**, 1913–1920; (b) M. Garbe, K. Junge, S. Walker, Z. H. Wei, H. J. Jiao, A. Spannenberg, S. Bacumann and M. Beller, *Angew. Chem., Int. Ed.*, 2017, **56**, 11237–11241.

9 (a) N. Abbas, Y. B. Wan and X.-P. Hu, *J. Org. Chem.*, 2025, **90**, 9667–9671; (b) Y. Y. Li, K. Lu, J. S. Yang, X. M. Zhang, F. M. Zhang and Y. Q. Tu, *Nat. Commun.*, 2025, **16**, 6078; (c) J. Yang, Y. Guo, Z. Wang, Y. Fu, D. Wang, Q. Liu, G. A. Solan, Y. Ma and W. H. Sun, *Org. Lett.*, 2025, **27**, 2564–2568; (d) S. Paira, N. Jain, D. Adhikari, R. B. Sunoj and B. Sundararaju, *Chem. Sci.*, 2025, **16**, 13826–13837; (e) Z. M. Wang, M. H. Li and W. W. Zuo, *J. Am. Chem. Soc.*, 2024, **146**, 26416–26426.

10 E. S. Wiedner, M. B. Chambers, C. L. Pitman, R. M. Bullock, A. J. M. Miller and A. M. Appel, *Chem. Rev.*, 2016, **116**, 8655–8692.

11 (a) R. A. Grey, G. P. Pez and A. Wallo, *J. Am. Chem. Soc.*, 1980, **102**, 5948–5949; (b) R. A. Grey, G. P. Pez, A. Wallo and J. Corsi, *J. Chem. Soc. Chem. Commun.*, 1980, **16**, 783–784; (c) G. P. Pez, R. A. Grey and J. Corsi, *J. Am. Chem. Soc.*, 1981, **103**, 7528–7535; (d) R. A. Grey, G. P. Pez and A. Wallo, *J. Am. Chem. Soc.*, 1981, **103**, 7536–7542; (e) R. A. Grey, G. P. Pez, A. Wallo and J. Corsi, *Ann. N. Y. Acad. Sci.*, 1983, **415**, 235–243.

12 (a) M. Nielsen, E. Alberico, W. Baumann, H.-J. Drexler, H. Junge, S. Gladiali and M. Beller, *Nature*, 2013, **495**, 85–89; (b) E. Alberico, A. J. J. Lennox, L. K. Vogt, H. Jiao, W. Baumann, H.-J. Drexler, M. Nielsen, A. Spannenberg, M. P. Checinski, H. Junge and M. Beller, *J. Am. Chem. Soc.*, 2016, **138**, 14890–14904; (c) C. Liu, R. V. Putten, P. O. Kulyaev, G. A. Filonenko and E. A. Pidko, *J. Catal.*, 2018, **363**, 136–143.

13 (a) R. Hartmann and P. Chen, *Angew. Chem., Int. Ed.*, 2001, **40**, 3581–3585; (b) R. Hartmann and P. Chen, *Adv. Synth. Catal.*, 2003, **345**, 1353–1359.

14 P. A. Dub, N. J. Henson, R. L. Martin and J. C. Gordon, *J. Am. Chem. Soc.*, 2014, **136**, 3505–3512.

15 (a) J. M. John, S. Takebayashi, N. Dabral, M. Miskolzie and S. H. Bergens, *J. Am. Chem. Soc.*, 2013, **135**, 8578–8584; (b) S. Nakane, T. Yamamura, S. K. Manna, S. Tanaka and M. Kitamura, *ACS Catal.*, 2018, **8**, 11059–11075.

16 (a) J. M. Hayes, E. Deydier, G. Ujaque, A. Lledos, R. M. Kabbara, E. Manoury, S. Vincendeau and R. Poli, *ACS Catal.*, 2015, **5**, 4368–4376; (b) P. Kisten, S. Vincendeau, E. Manoury, J. M. Lynam, J. M. Slattery, S. B. Duckett, A. Lledos and R. Poli, *Chem. Sci.*, 2024, **15**, 20478–20492.

17 (a) Y. Wang, S. Liu, H. Yang, H. Li, Y. Lan and Q. Liu, *Nat. Chem.*, 2022, **14**, 1233–1241; (b) C. Yin, F. Jiang, Y. F. Huang, C. Q. Xu, Y. Pan, S. Gao, G. Q. Chen, X. Ding, S. T. Bai, Q. Lang, J. Li and X. Zhang, *Nat. Commun.*, 2023, **14**, 3718; (c) M. Wang, S. Liu, H. Liu, Y. Wang, Y. Lan and Q. Liu, *Nature*, 2024, **631**, 556–562.

18 (a) K. P. Manfredi, J. W. Blunt and J. H. Cardellina, *J. Med. Chem.*, 1991, **34**, 3402–3405; (b) M. R. Boyd, Y. F. Hallock and K. P. Manfredi, *J. Med. Chem.*, 1994, **37**, 1740–1745; (c) G. Bringmann, T. Gulder and T. A. M. Gulder, *Chem. Rev.*, 2011, **111**, 563–639; (d) L. Pu, *Chem. Rev.*, 2004, **104**, 1687–1716; (e) G. Dotsevi, Y. Sogah and D. J. Cram, *J. Am. Chem. Soc.*, 1976, **98**, 3038–3041; (f) Q. Li, L. Green and N. Venkataraman, *J. Am. Chem. Soc.*, 2007, **129**, 12908–12909; (g) M. Berthod, G. Mignani and G. Woodward, *Chem. Rev.*, 2005, **105**, 1801–1836; (h) M. Shibasaki and S. Matsunaga, *Chem. Soc. Rev.*, 2006, **35**, 269–279; (i) B. V. Rokade and P. J. Guiry, *ACS Catal.*, 2018, **8**, 624–643.

19 (a) S. J. Liu, X. Wang, J. X. Yang, X. S. Ao, S. F. Ni, Y. C. Zhang and F. Shi, *Nat. Commun.*, 2025, **16**, 6605; (b) H. H. Zhang, T. Z. Li, S. J. Liu and F. Shi, *Angew. Chem., Int. Ed.*, 2024, **63**, e202311053; (c) H. Liu, Z. Qi, Y. Shi, W. Wang, F. Wang, Z. W. Ding, A. Q. Jia, G. Huang and X. Li, *Nat. Commun.*, 2025, **16**, 5741; (d) D. K. Janabel, V. V. Kanale, M. Liu and C. Uyeda, *J. Am. Chem. Soc.*, 2025, **147**, 23270–23276; (e) Q. Bian, L. Qin, L. W. Fan, J. Fu, Y. F. Cheng, Y. F. Zhang, Q. Song, P. F. Wang, Z. L. Li, Q. S. Gu, P. Yu, J. B. Tang and X. Y. Liu, *Nat. Commun.*, 2025, **16**, 4922; (f) J. M. Coto-Cid, G. de Gonzalo, J. A. Carmona, J. Iglesias-Sigüenza, P. Rodríguez-Salamanca, R. Fernández, V. Hornillos and J. M. Lassaletta, *Adv. Synth. Catal.*, 2024, **366**, 909–915; (g) X. Hao, Z. Tian, Z. Yao, T. Zang, S. Song, L. Lin, T. Qiao, L. Huang and H. Fu, *Angew. Chem., Int. Ed.*, 2024, **63**, e202410112; (h) L. L. Dai, Y. Liu, Q. Xu, M. Wang, Q. Zhu, P. Yu, G. Zhong and X. Zeng, *Angew. Chem., Int. Ed.*, 2023, **62**, e202216534; (i) Y.-D. Shao, D.-D. Han, H.-X. Jiang, X.-Y. Zhou, W.-K. Wang, J.-X. Zhang, Y.-F. Liu and D.-J. Cheng, *Org. Chem. Front.*, 2024, **11**, 3894–3899; (j) P. Rodríguez-Salamanca, G. de Gonzalo, J. A. Carmona, J. López-Serrano, J. Iglesias-Sigüenza, R. Fernández, J. M. Lassaletta and V. Hornillos, *ACS Catal.*, 2022, **13**, 659–664; (k) D. Y. Wang, J. Y. Zong, B. W. Wang, L. W. Sun, X. Xiao, H. R. Piao and F. E. Chen, *Green Synth. Catal.*, 2025, **6**, 211–215.

20 (a) G. Q. Chen, B. J. Lin, J. M. Huang, L. Y. Zhao, Q. S. Chen, S. P. Jia, Q. Yin and X. Zhang, *J. Am. Chem. Soc.*, 2018, **140**, 8064–8068; (b) Y.-B. Wan and X.-P. Hu, *ACS Catal.*, 2022, **14**, 17633–17641; (c) T. Niu, L.-X. Liu, Y.-Q. Bai, H.-W. Li, B. Wu and Y.-G. Zhou, *Sci. China: Chem.*, 2025, **68**, 4984–4990.

21 (a) F. Ling, S. Nian, J. Chen, W. Luo, Z. Wang, Y. Lv and W. Zhong, *J. Org. Chem.*, 2018, **83**, 10749–10761; (b) F. Ling, H. Hou, J. Chen, S. Nian, X. Yi, Z. Wang, D. Song and W. Zhong, *Org. Lett.*, 2019, **21**, 3937–3941; (c) X. Yi, Y. Chen, A. Huang, D. Song, J. He, F. Ling and W. Zhong, *Org. Chem. Front.*, 2021, **8**, 6830–6836; (d) Z. Wang, X. Zhao, A. Huang, Z. Yang, Y. Cheng, J. Chen, F. Ling and W. Zhong, *Tetrahedron Lett.*, 2021, **82**, 153389.

22 V. Hornillos, J. A. Carmona, A. Ros, J. Iglesias-Siguenza, J. Lopez-Serrano, R. Fernandez and J. M. Lassaletta, *Angew. Chem., Int. Ed.*, 2018, **57**, 3777–3781.

23 (a) X. Hong, J. Guo, J. Liu, W. Cao, C. Wei, Y. Zhang, X. Zhang and Z. Fu, *Sci. China: Chem.*, 2022, **65**, 905–911; (b) Y. Chen, Y. Cheng, W. Tong, H. Wu, C. Zhao, D. Song, F. Ling and W. Zhong, *Green Chem.*, 2025, **27**, 7717–7727; (c) M. Zhang,

T. Niu, M. Liang, F. Xu, Y. Du, H. Zhuang, R. J. Song, H. Yang and Q. Yin, *J. Am. Chem. Soc.*, 2025, **147**, 18197–18207; (*d*) M. Liao, J. Li, H. Zhu, Z. Han, Y. Zhang, J. Sun and H. Huang, *Org. Lett.*, 2025, **27**, 4836–4841.

24 (*a*) X. Han, F. Zhong, Y. Wang and Y. Lu, *Angew. Chem., Int. Ed.*, 2012, **51**, 767–770; (*b*) X. Xiao, B. Shao, J. Li, Z. Yang, Y. J. Lu, F. Ling and W. Zhong, *Chem. Commun.*, 2021, **57**, 4690–4693; (*c*) N. Abbas, Y. B. Wan and X. P. Hu, *J. Org.* *Chem.*, 2025, **90**, 9667–9671; (*d*) J. Yang, Y. Guo, Z. Wang, Y. Wang, D. Fu, Q. Liu, G. A. Solan, Y. Ma and W. H. Sun, *Org. Lett.*, 2025, **27**, 2564–2568; (*e*) L. Z. Zhang, P. C. Zhang, Q. Wang, M. Zhou and J. Zhang, *Nat. Commun.*, 2025, **16**, 930.

25 CCDC 2455680: Experimental Crystal Structure Determination, 2025, DOI: 10.5517/ccdc.csd.cc2nfbhy.